A&A, 710, A408 (2026)
https://doi.org/10.1051/0004-6361/202659563

Astronomy & Astrophysics

XRISM/Resolve probes a possible "raining" absorber in Mrk 509

M. Dadina[1,★], V. Missaglia[1], V. Braito[2], M. Cappi[1], A. Luminari[3,4], D. Barret[5], E. Bertola[6], S. Bianchi[7], A. Comastri[1], G. Chartas[8], J. Kaastra[9,10], E. Kammoun[11], G. Lanzuisi[1], G. Matzeu[12], R. Middei[3,13], E. Nardini[6], F. Nicastro[3], P.-O. Petrucci[14], C. Pinto[15], R. Serafinelli[16,3], A. Tortosa[3], and C. Vignali[1,17]

[1] INAF – Osservatorio di Astrofisica e Scienza dello Spazio di Bologna, Via Gobetti 101, I-40129 Bologna, Italy
[2] INAF – Osservatorio Astronomico di Brera, Via Bianchi 46, I-23807 Merate (LC), Italy
[3] INAF – Osservatorio Astronomico di Roma, Via Frascati 33, I-00078 Monte Porzio Catone, Italy
[4] INAF – Istituto di Astrofisica e Planetologia Spaziali, via Fosso del Cavaliere 100, I-00133 Roma, Italy
[5] Institut de Recherche en Astrophysique et Planétologie, 9 avenue du Colonel Roche, Toulouse 31028, France
[6] INAF – Osservatorio Astrofisco di Arcetri, largo E. Fermi 5, 50127 Firenze, Italy
[7] Dipartimento di Matematica e Fisica, Università degli Studi Roma Tre, Via della Vasca Navale 84, I-00146 Roma, Italy
[8] Department of Physics and Astronomy, College of Charleston, Charleston, SC 29424, USA
[9] SRON Netherlands Institute for Space Research, Leiden, The Netherlands
[10] Leiden Observatory, University of Leiden, P.O. Box 9513, NL-2300 RA Leiden, The Netherlands
[11] Cahill Center for Astronomy & Astrophysics, California Institute of Technology, 1216 East California Boulevard, Pasadena, CA 91125, USA
[12] Quasar Science Resources SL for ESA, European Space Astronomy Centre (ESAC), Science Operations Department, 28692 Villanueva de la Cañada, Madrid, Spain
[13] Space Science Data Center, Agenzia Spaziale Italiana, Via del Politecnico snc, 00133 Roma, Italy
[14] Université Grenoble Alpes, CNRS, IPAG, 38000 Grenoble, France
[15] INAF–IASF Palermo, Via U. La Malfa 153, I-90146 Palermo, Italy
[16] Instituto de Estudios Astrofísicos, Facultad de Ingeniería y Ciencias, Universidad Diego Portales, Av. Ejército Libertador 441, Santiago, Chile
[17] Dipartimento di Fisica e Astronomia 'Augusto Righi', Università degli Studi di Bologna, Via Gobetti 93/2, I-40129 Bologna, Italy

Received 23 February 2026 / Accepted 4 May 2026

ABSTRACT

Context. X-ray spectroscopy of active galactic nuclei (AGNs) offers unique insights into the reprocessing of radiation and the gas dynamics near supermassive black holes. The Seyfert 1 galaxy Mrk 509 is an ideal laboratory for these studies. It is in fact known for its complex iron K emission and one of the four or five AGNs to date in which evidence of transient, blue- and redshifted absorption features indicative of high-velocity flows has been detected in X-rays.
Aims. We present the first high-resolution 2–10 keV spectrum of Mrk 509 obtained with the *XRISM*/Resolve calorimeter. Our primary goals are to disentangle the narrow and broad emission features and to place stringent constraints on the kinematics and physical locations of circumnuclear gas flows, specifically searching for signatures of accretion and feedback.
Methods. We analyzed 106 ks of XRISM/Resolve data, complemented by simultaneous *XMM-Newton* and *NuSTAR* observations, which we used to constrain the broadband continuum. We modeled the spectra using self-consistent reflection models for the continuum and the emission lines, and employed photoionized plasma models to characterize discrete, ionized absorption features.
Results. The XRISM/Resolve spectrum reveals a narrow Fe Kα core resolved with $\sigma \simeq 10$ eV ($v_{\rm FWHM} \sim 1100$ km/s). The best-fit model includes a broader component with $\sigma \sim 450$ eV. We also find tentative evidence of discrete absorption features at rest-frame energies of $E \sim 6.2$ keV. When modeled as an ionized absorber (with a significance of ~3.6σ), the data suggest the gas is redshifted relative to the systemic velocity, corresponding to an inflow of material with $v_{\rm in} \sim 11\,000$ km s^{-1}, located within the inner few thousand gravitational radii.
Conclusions. The narrow Fe Kα emission is consistent with an origin in the dusty torus, while the broad component arises from broad-line-region scales or the accretion disk ($R \sim 30$–$120\,r_g$). This scenario is strongly corroborated by our relativistic reflection modeling, which restricts the inner edge of the emitting region to distances greater than 27 r_g. If confirmed by future observations, the high-velocity inflow would likely represent dense, fragmented clumps of a "failed wind" raining back onto the accretion disk, providing potential direct evidence that nonstandard accretion processes may coexist with canonical disk-like flows in the inner regions of AGNs.

Key words. galaxies: active – galaxies: individual: Mrk509 – galaxies: Seyfert – X-rays: galaxies

1. Introduction

X-ray spectroscopy of active galactic nuclei (AGNs) provides an unparalleled tool for probing the extreme environments surrounding supermassive black holes (SMBHs), which are believed to coevolve with their host galaxies (e.g., Kormendy & Ho 2013; Heckman & Best 2014). Among the features observed, the iron Kα (Fe Kα) emission line at 6.4 keV is nearly ubiquitous and serves as a powerful tracer of circumnuclear gas (Nandra et al. 2007). The line's profile is a key diagnostic of its physical origin: a narrow core is typically associated with reflection from distant material, such as the molecular torus

★ Corresponding author: mauro.dadina@inaf.it

(see Antonucci 1993), while a broad and relativistically skewed profile is the hallmark of emission from the inner accretion disk, just a few gravitational radii ($r_g = \frac{GM}{c^2}$, where G is the gravitational constant, M is the mass of the SMBH, and c is the speed of light) from the SMBH (e.g., Tanaka et al. 1995; Fabian et al. 2000).

In addition to emission, AGN spectra often exhibit absorption features from ionized gas along the line of sight. Blueshifted absorption lines are clear signatures of outflows, with the most extreme examples being the ultrafast outflows (UFOs) that reach velocities up to $v \sim 0.1$–$0.5c$ (e.g., Chartas et al. 2002, 2021; Pounds et al. 2003; Reeves et al. 2002, 2009, 2014, 2018; Dadina et al. 2005, 2018; Cappi 2006; Cappi et al. 2009; Tombesi et al. 2010, 2011, 2013; Gofford et al. 2013; Nardini et al. 2015; Matzeu et al. 2016, 2017, 2023; Braito et al. 2018; Gianolli et al. 2024; Xrism Collaboration 2025a). These powerful winds are considered a key channel for AGN feedback, regulating SMBH growth and star formation (e.g., King & Pounds 2015; Gaspari et al. 2020; Laha et al. 2021). Conversely, redshifted absorption features, indicative of infalling material, remain far rarer. Only a small number of candidate ultrafast inflows (UFIs) exist in the literature (e.g., Nandra et al. 1999; Dadina et al. 2005; Yaqoob & Serlemitsos 2005; Longinotti et al. 2007; Giustini et al. 2017; Peca et al. 2025). Ultrafast inflows offer a unique window into nonstandard accretion processes, such as fallback from "aborted jets" or "failed winds", where the launched material fails to escape the SMBH's gravitational pull (e.g., Ghisellini et al. 2004; Proga & Kallman 2004; Giustini & Proga 2019).

The bright, nearby Seyfert 1 galaxy Mrk 509 ($z = 0.034$, Huchra et al. 1993) is an ideal laboratory for studying these phenomena. Extensive monitoring has revealed a complex Fe Kα structure composed of a constant narrow core and a variable, resolved component (Ponti et al. 2013). Reverberation mapping has shown that the resolved component responds to continuum variations on timescales of days, placing its origin within a few light-days from the central engine (Ponti et al. 2013). Furthermore, Mrk 509 is one of the very few objects where transient, redshifted Fe K absorption lines–the potential signature of a UFI–have been reported in the literature (Dadina et al. 2005). The source has also shown evidence of variable, highly ionized outflows with velocities up to ~14 000 km s^{-1} (Dadina et al. 2005; Ponti et al. 2009; Cappi et al. 2009; Tombesi et al. 2010).

In this work, we present the first high-resolution X-ray spectrum of Mrk 509 ($M_{BH} \sim 1.02 \times 10^8\, M_\odot$, Li et al. 2024) in the 2–10 keV band, obtained with the Resolve (Ishisaki et al. 2025) instrument on board the X-Ray Imaging and Spectroscopy Mission (*XRISM*, Tashiro et al. 2024). Leveraging the unprecedented spectral resolution of Resolve (≈4.7 eV at 6 keV, Ishisaki et al. 2025), our analysis aims to disentangle the complex emission and absorption features in the Fe K band. This will allow us to place new, stringent constraints on the physical properties, dynamics, and location of the different gas flows, from the reverberating reflector to the transient inflows and outflows.

The approved *XRISM* observation of Mrk 509 (P.I. M. Cappi) was designed with three primary scientific goals: *i)* confirming and studying gas in- and outflows, *ii)* defining the origin of the neutral Fe Kα line, and *iii)* understanding the origin of the ionized iron complex. The *XRISM* proposal triggered the organization of a broader, complementary multiwavelength campaign with the *NuSTAR*, *XMM-Newton*, Swift, and optical telescopes (NTT/TNG) to provide a complete view of the source. However, in this work, we focus mainly on the results obtained analyzing the *XRISM*/Resolve data and taking advantage of the *XMM-Newton* (Jansen et al. 2001) and *NuSTAR* (Harrison et al. 2013) capabilities to define the baseline X-ray continuum of Mrk 509. The broadband properties of the source, including the spectral complexities in the soft energy band and the source variability, will be addressed in an upcoming paper (Missaglia et al., in prep.).

Table 1. Observation log with net exposure times.

Instr#	Obs. Starting Date	Exp (ks)
XRISM	2024/11/12	106
NuSTAR#1	2024/11/12	12.5
XMM#1	2024/11/12	17.2
XMM#2	2024/11/13	9.2
XMM#3	2024/11/14	30.7
NuSTAR#2	2024/11/15	21.2

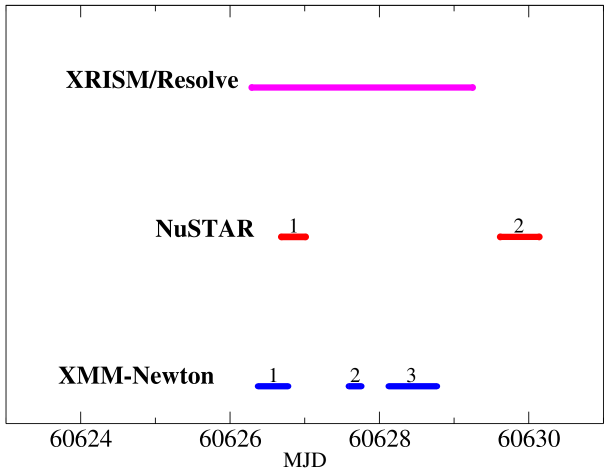

Fig. 1. Time scheme of the X-ray observation presented in this work. The horizontal lines represent the total observation times.

2. Data reduction and analysis

XRISM observed Mrk 509 on November 11, 2024. The high-resolution Resolve calorimeter operated in its standard PX NORMAL mode. We were unable to use the Xtend data due to a camera anomaly during this observation. While prior studies with missions such as *XMM-Newton* and *Chandra* have characterized Mrk 509 at CCD resolutions, this work focuses primarily on the new, high-resolution Resolve spectrum. Nonetheless, we also present an analysis of the *NuSTAR* and *XMM-Newton* data collected via DDT observations triggered to coordinate with the *XRISM*/Resolve pointing. These data are particularly important for properly constraining the continuum emission in the 2–10 keV band. The source was observed twice with *NuSTAR* in November 2024 for a total exposure of ~34 ks. Quasi-simultaneous observations (three in total) were also performed with *XMM-Newton*. Table 1 lists the details of all observations, while Fig. 1 displays the temporal coverage of each pointing.

The *XRISM*/Resolve data were reduced using the *XRISM* Quick-Start Guide v2.3, HEASOFT version 6.34, and the associated calibration files. Briefly, the data were filtered to exclude anomalies in low-Earth orbit as well as events from

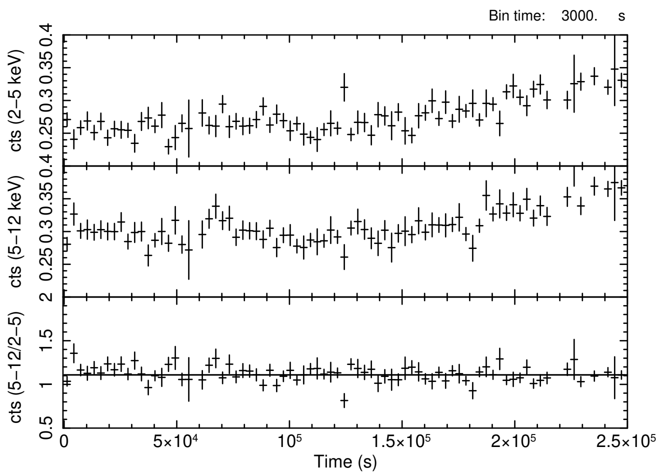

Fig. 2. Non-background-subtracted *XRISM*/Resolve light curves of Mrk 509 shown in the 2–5 keV (top panel) and 5–12 keV (middle panel) energy bands. Bottom: Corresponding hardness ratio. A clear brightening trend is evident toward the end of the observation, but it is not accompanied by significant spectral variability.

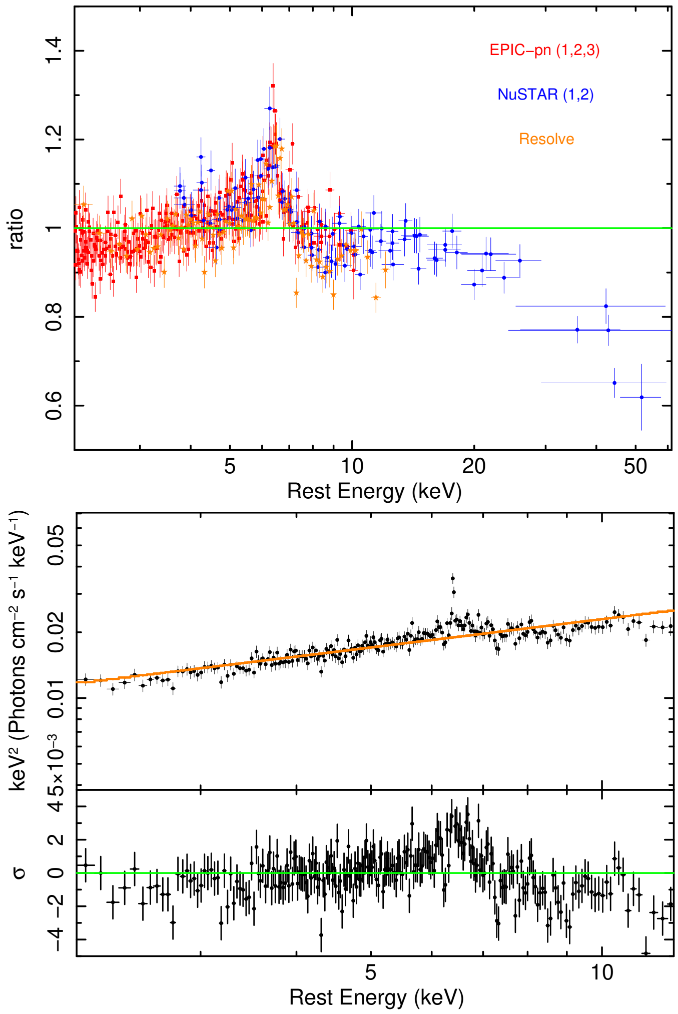

Fig. 3. *Upper panel*: 2–60 keV ratio between the data and a simple power-law model for the Mrk 509 X-ray data taken during this campaign (see Table 1), expressed in units of standard deviations. Here, for clarity purposes, the data have been strongly rebinned (each data point has a 25σ significance). *Lower panel*: 2–12 keV spectrum of Mrk 509 observed by *XRISM*/Resolve. The orange line represents the best fit using a simple power-law model. In this case, the Resolve data have also been rebinned (each data point here has a significance of 15σ) for visual clarity.

the calibration pixel (pixel 12) and pixel 27 with abnormal gain behavior. The data were further screened to include only high-resolution primary (Hp) events. The technical report from the instrument team confirms the nominal functioning of the Resolve instrument during the observation, with an energy resolution of ~4.6 eV at the Fe^{55} reference energy, and no gain shift was detected over the course of the exposure. A light curve of the event list reveals flux variability, with distinct brightening during the final third of the observation (see Fig. 2). A search for spectral variability, performed by analyzing the ratio between the 2–5 keV and 5–12 keV bands, indicates no strong spectral variability associated with this change in flux (see Fig. 2). For this reason, a time-averaged spectral analysis is well justified. The resulting spectrum was built with default bins of 0.5 eV, and the tools rslmkrmf and xaarfgen were used to make the redistribution matrix file (rmf) and ancillary response file (arf). We elected to create a "Large" (Gaussian core plus exponential tail and Si Kα instrumental line plus escape peak) rmf. After screening (e.g., pixel-pixel coincident events), the net Resolve exposure time was approximately 106 ks. Finally, following standard procedure (see, for example, Xrism Collaboration 2025a), we treated the background by directly incorporating the generated non-X-ray background (NXB) into our spectral models.

We processed *XMM-Newton* EPIC-pn data using the Science Analysis System (SAS) v21.0. Calibrated event lists were generated from the raw observation data files (ODFs) using the standard pipeline chains. The camera was operated in small window mode to minimize photon pileup. The resulting event lists were filtered to remove periods of high particle background flaring, and standard pattern selection criteria were applied. For the spectral analysis, source counts were extracted from a 28″-radius circular region centered on the source's position. The background spectrum was estimated from two nearby, source-free 26″-radius circular regions located on the same CCD. The corresponding arfs and rmfs were generated for spectral fitting.

Similarly, we processed *NuSTAR* data for both observations using the NuSTAR Data Analysis Software (NuSTARDAS) package. Source spectra were extracted from a 1.5′-radius circular region centered on the target. For the background, we used a separate 1.88′-radius circular region located on the same detector, chosen to be free of source contamination. The nuproducts task was used to filter the data, apply standard screening criteria, and generate all final data products, including spectra and response files.

To prepare the data for spectral fitting, we applied specific grouping and band-pass selections for each instrument. The *XRISM*/Resolve data were analyzed in the 2–12 keV band to avoid calibration uncertainties at the spectral boundaries. Following Mizumoto et al. (2026), these data were uniformly grouped by a factor of 10, resulting in a final bin size of 5 eV (Tashiro et al. 2025). Although this slightly overbins the nominal energy resolution of Resolve, we adopted this conservative approach to enhance the signal-to-noise ratio (S/N) per spectral bin, facilitating both the detection and the modeling of weak and broad spectral features. Furthermore, the choice of a constant energy binning was dictated by the mathematical requirements of certain convolution models used in our analysis, such as `gsmooth` (see Sect. 4). Finally, we anticipate here that this choice does not strongly impact our data analysis, since the width of the narrow Fe emission line is found to be on the order of σ ~10 eV

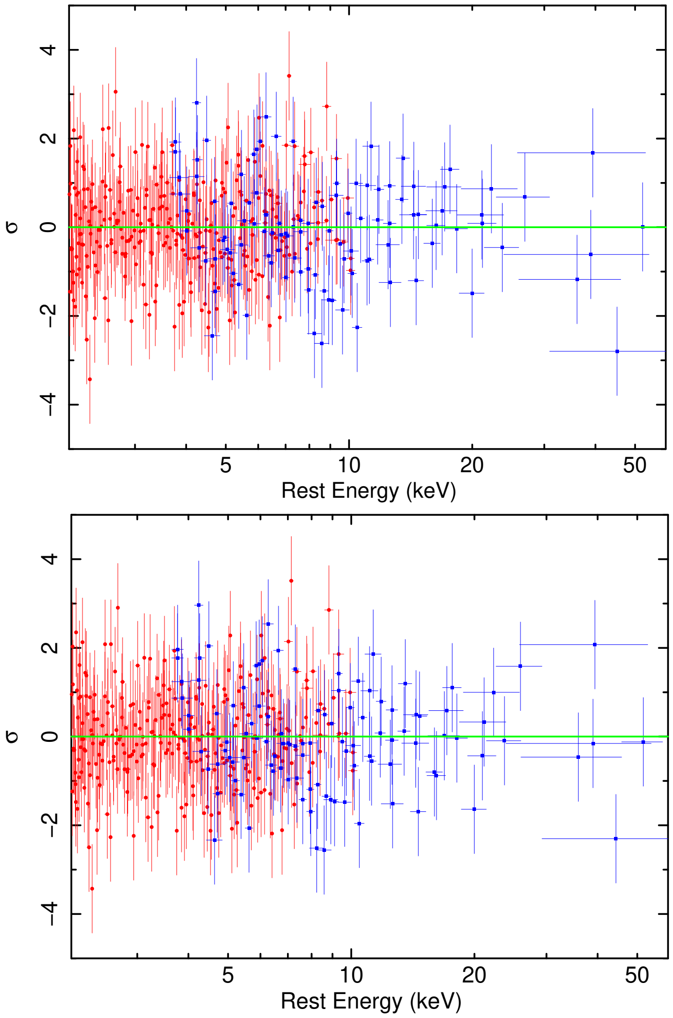

Fig. 4. *Upper panel*: Residuals of the PC2 model (neutral partial covering with distant reflection component). *Lower panel*: Residuals of the RR2 model (neutral partial covering with a relativistic reflection component and narrow Fe Kα Gaussian emission line). In all panels, the *XMM-Newton* data are in red, while the *NuSTAR* data are in blue.

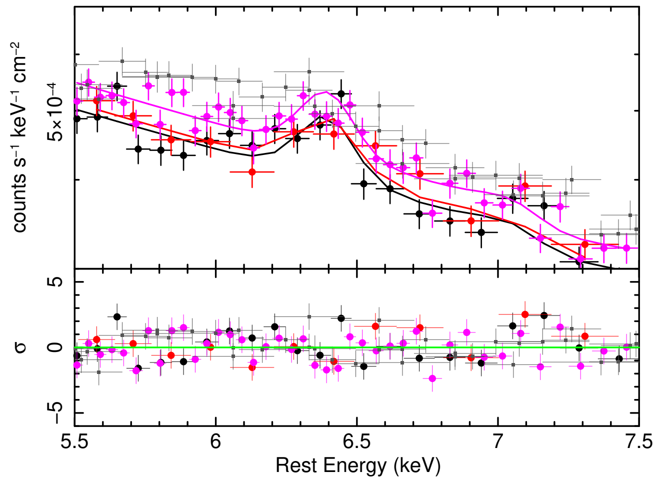

Fig. 5. Zoom-in on the 5.5–7.5 keV range PC2 model (see Table 2). XMM-Newton data observation 1 is in black, observation 2 is in red, and observation 3 is in magenta. The NuSTAR data are in gray. There are no significant residuals.

(see Sect. 4). The EPIC-pn data were grouped to a minimum of 100 counts per bin, while the *NuSTAR* data were similarly grouped to ensure a minimum of 50 counts per bin.

3. Defining a baseline model using the 2–60 keV XMM-Newton and NuSTAR data

A simple power-law model to simultaneously fit the 2–60 keV *XRISM*/Resolve, the *XMM-Newton*/EPIC-pn, and *NuSTAR* data reveals several key features (see Fig. 3, upper panel). The most prominent are: a) a narrow emission line centered at $E \approx 6.4$ keV and b) a broad excess spanning the 4–7 keV band.

To determine the best modeling of the continuum, we analyzed the 2–60 keV data from *XMM-Newton*/EPIC-pn and *NuSTAR* only. At this stage, we excluded the data below 2 keV to avoid the complexities associated with the known strong soft excess (see e.g., Mehdipour et al. 2011; Petrucci et al. 2013, 2018) and the complex warm absorber (Kaastra et al. 2012) that strongly affect the low energy ($E \leq 2$ keV) spectrum of Mrk 509.

The spectral analysis, including all *NuSTAR* and EPIC-pn datasets collected during our campaign (total of five observations; see Table 1), was performed using the XSPEC fitting package v12.15.1 (Arnaud et al. 1999). We included a cross-normalization constant to account for differences in absolute calibration between the instruments, as well as for intrinsic source variability (see columns X-XIII in Table 2). Mrk 509 is known to exhibit X-ray flux variations on typical timescales of days (Kumari et al. 2021). This behavior is indeed confirmed by the *XRISM*/Resolve light curves (see Fig. 2).

We started using a simple cutoff power-law model plus a Gaussian emission line to reproduce the Fe Kα feature. The high-energy cutoff was fixed at a fiducial value of $E_c = 150$ keV (see Petrucci et al. 2013), as the current data do not provide meaningful constraints on this parameter. We fixed the line width to $\sigma = 20$ eV, consistent with the narrow feature clearly resolved in the *XRISM*/Resolve data (see both panels of Fig. 3).

The energy of the Gaussian is found to be consistent with neutral iron ($E = 6.39 \pm 0.02$). If we model the remaining curvature observed in the 4–7 keV band with a broad Gaussian, we find that its centroid is at $E \sim 5.4$ keV with a width of $\sigma \sim 1.5$ keV. This hence indicates that the underlying continuum may be poorly described by simple power-law modeling. We also fixed the broad Gaussian to the same energy of the narrow component; however, residuals remain.

To describe the residual spectral curvature observed at 4–7 keV, we explored different scenarios using different continuum models. These include i) a neutral, partial absorber (models PC1 and PC2 in Table 2) and/or ii) a relativistic scenario due to reflection from material in the disk (models RR1-RR2 with `relxill` in Table 2).

The partial covering models provide a robust description of the broadband data. Specifically, when a simple Gaussian line is added, the feature is found to be consistent with emission from cold material (see the PC1 model in Table 2). Furthermore, motivated by the *XRISM*/Resolve spectra (see Sect. 4)–which clearly reveal a narrow core–we tested a scenario where this component originates from neutral reflection from distant material (modeled using `pexmon`, Nandra et al. 2007). This approach significantly improves the quality of the fit (see model PC2 in Table 2). Finally, we tested for an additional broad Fe Kα Gaussian component but found it statistically unnecessary when adopting the partial covering model. This modeling, moreover, allows us to recover photon index values ($\Gamma \sim 1.7$) in

Table 2. Best-fits of the *XMM-Newton* EPIC-pn plus *NuSTAR* data.

Model	Γ	N_H (10^{22} cm^{-2})	C_f	$E_{FeK\alpha}$ (keV)	R	σ (eV)	EW (eV)	C/d.o.f.	$C_{pn,2}$	$C_{pn,3}$	$C_{FPMA/B,1}$	$C_{FPMA/B,2}$
PC1	1.65 ± 0.02	12.5 ± 1.7	0.23 ± 0.02	6.39 ± 0.03	–	102 ± 40	68 ± 3	2555/2422	1.03 ± 0.01	1.11 ± 0.02	1.24 ± 0.02	1.27 ± 0.02
PC2	1.76 ± 0.02	12.1 ± 1.2	0.31 ± 0.03	–	0.38 ± 0.04	–	–	2529/2424	1.03 ± 0.01	1.11 ± 0.01	1.24 ± 0.02	1.27 ± 0.02

Model	N_H (10^{22} cm^{-2})	C_f	Γ	r_{in} (ISCO)	$\log \xi$	R	a	C/d.o.f.	$C_{pn,2}$	$C_{pn,3}$	$C_{FPMA/B,1}$	$C_{FPMA/B,2}$
RR1	–	–	$1.47^{+0.01}_{-0.01}$	1*	$4.28^{+0.05}_{-0.09}$	$0.74^{+0.48}_{-0.21}$	>0.85	2683/2422	1.03 ± 0.01	1.11 ± 0.01	1.24 ± 0.02	1.27 ± 0.02
RR2	10.35 ± 2.10	$0.20^{+0.04}_{-0.02}$	$1.59^{+0.08}_{-0.04}$	1*	$3.56^{+0.20}_{-0.68}$	$0.41^{+0.39}_{-0.24}$	0.99^{u}	2519/2420	1.03 ± 0.01	1.11 ± 0.01	1.24 ± 0.02	1.27 ± 0.02

Notes. *Upper table:* Col. I: Model name; Col. II: Photon index of the primary emission; Col. III: Column density of the partial absorber; Col. IV: Covering factor; Col. V: Energy of the emission line; Col. VI: direct-to-reflected continuum ratio; Col. VII: Width of the emission line; Col. VIII: Equivalent width of the emission line; Col. IX: Cash statistics over degrees of freedom. *Lower table:* Col. I: Model name; Col. II: Column density of the partial absorber; Col. III: Covering factor; Col. IV: Photon index of the primary emission; Col. V: Inner radius of the accretion disk; Col. VI: Ionization of the accretion disk; Col. VII: Reflection fraction parameter; Col. VIII: Spin of the BH; Col. IX: Cash statistics over degrees of freedom. Cols. X-XIII: Cross-normalization constants between *XMM-Newton* EPIC-pn and *NuSTAR*. Reported errors are at the 90% confidence level. In models RR1-RR2, the line energy and σ are fixed at 6.4 keV and 20 eV, respectively. Model PC1: constant × TBabs × zpcfabs(cutoffpl + line); Model PC2: TBabs(cutoffpl + pexmon + (1 + constant) × zTBabs(cutoffpl)); Model RR1: constant × TBabs(zgauss + relxill), with Rbr = 15, AFe = 1; Model RR2: constant × TBabs × zpcfabs(relxill + zgauss).

agreement with those previously reported in literature ($\Gamma \sim$ 1.6–1.7; Pounds et al. 2001; Ponti et al. 2009, 2013) and with the average value found in AGN samples (Nandra & Pounds 1994; Piconcelli et al. 2005; Dadina 2007, 2008; Bianchi et al. 2009; Ricci et al. 2017; Middei et al. 2019).

To test the relativistic reflection scenario, we initially applied a model consisting of a relativistic reflection component (`relxill`, Dauser et al. 2014) and a narrow Fe Kα Gaussian emission line. As in the previous case, we fixed the high-energy cutoff to E_c = 150 keV and, as shown in Petrucci et al. (2013), we fixed the inclination angle of the system at Θ = 30°. This baseline model provides a poor description of the data (model RR1 in Table 2), leaving significant positive residuals. Similarly to the simple power-law model, the inclusion of a partial covering component is also required (model RR2 in Table 2). This addition significantly improves the fit (see residuals in the lower panel of Fig. 4). Left free to vary, the black hole spin (indicated by the a parameter in Table 2) remains unconstrained, while the reflection component is consistent with that measured in the PC2 model. Following the approach adopted for model PC2, we also tested a scenario where the narrow Fe Kα line originates from the distant torus (modeled using `pexmon`). This resulted in a significantly poorer fit to the data than model RR2. Finally, it is worth noting that in all these relativistic scenarios, the recovered photon index of the primary emission is consistently flat (see Table 2).

As reported in Table 2, the PC2 and RR2 models provide the best fits to the broadband data (see also the two panels in Fig. 5 for a zoom-in on the residuals in the Fe K band for the PC2 and RR2 best fits). The RR2 scenario introduces four additional free parameters but provides only marginal statistical improvement (ΔC = 10) and, crucially, the PC2 model yields a primary photon index in perfect agreement with values typically observed in Seyfert galaxies (Nandra & Pounds 1994; Ricci et al. 2017). In the latter scenario, we assume that the reflection component originates in the torus, as suggested by the narrowness of the Fe K features (see also Section 4). Consequently, in our model, this component is not affected by the partial absorber, which is assumed to cover only the emission originating in the Mrk 509 core.

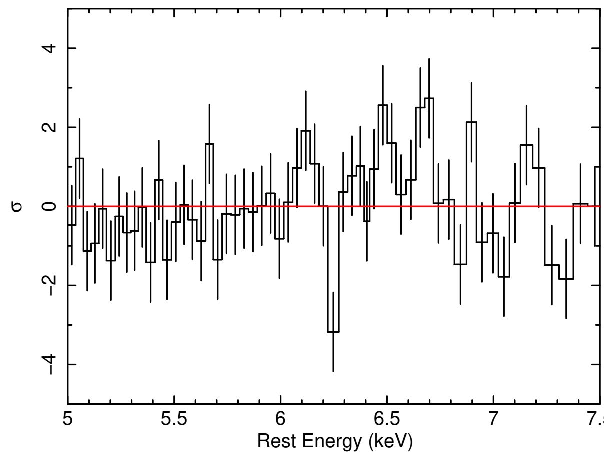

Fig. 6. 5–7.5 keV zoom-in on the Resolve residuals for the model including cold partial covering and the zFeKlor component to account for the narrow Fe Kα complex. The data are strongly rebinned for clarity purposes (each data point in the plot has a 20σ significance). The most significant deviations from the model are a possible absorption feature at $E \sim$ 6.2 keV and a broader component in the 6–6.8 keV range.

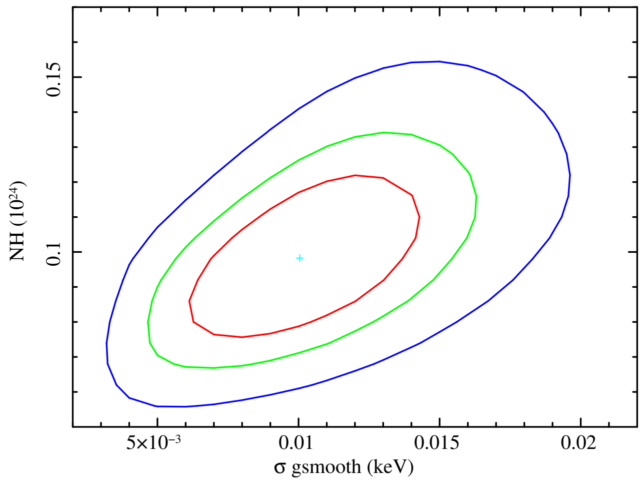

Fig. 7. Confidence contours between the column density and broadening kernel for the distant reflector from MYTorus modeling of the reflector and associated lines (see Sect. 4.1).

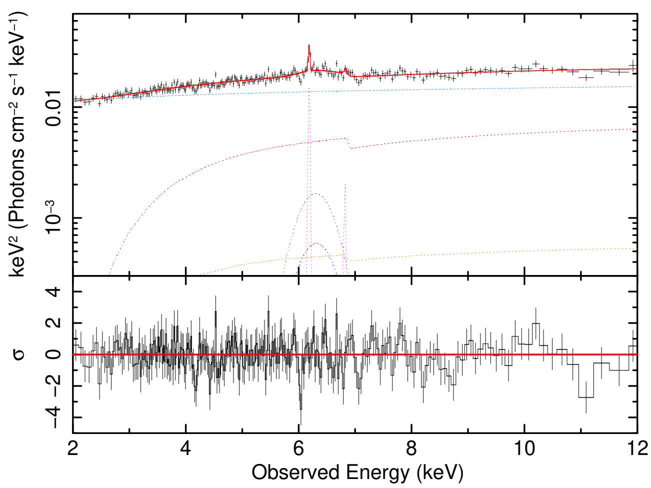

Fig. 8. 2–12 keV spectrum of Mrk 509 modeled with partial covering of the primary emission, broad Gaussian line, and neutral reflection (`MYTorus` model; see model I in Table 3). The components are shown as dotted lines: absorbed power-law (red), absorbed broad Gaussian line (blue), MYTorusL (magenta), and MYTorusS (orange).

4. The XRISM/Resolve view of the Fe complex

Building on the results presented above, we tested both the simple partial covering model (named PC in the following) and the relativistic scenario (named RR in the following) on our *XRISM*/Resolve data. Starting with the PC2 scenario, we used a simple `zpcfabs` model (see Sect. 3), yielding a canonical photon index of $\Gamma \sim 1.8$, in excellent agreement with the values obtained from *XMM-Newton* EPIC-pn and *NuSTAR* data. In this scenario, the primary emission is partially absorbed (covering fraction $C_f \sim 0.3$) by a neutral component with a column density of $N_H \sim 1.3 \times 10^{23}$ cm^{-2} (again consistent with the broadband fit obtained, as discussed in Sect. 3).

The narrow Fe Kα line was modeled using the `zFeklor` model (this model includes seven Lorentzian profiles to describe the line; see Hölzer et al. 1997). The energy centroid of this model is not a free parameter in the fit. When its redshift is allowed to vary, the best fit is obtained at $z = 0.03389^{+0.00072}_{-0.00025}$ (errors correspond to the 90% confidence level here and throughout the paper, unless stated otherwise), which is in good agreement with the redshift of the source. To estimate the line width, we applied a `gsmooth` convolution model to the `zFeklor` component, yielding $\sigma_n = 10 \pm 5$ eV and an equivalent width of $EW_n \sim 27$ eV. These parameters strongly suggest that this feature originates far from the central SMBH.

Some residuals remain at the rest energy of the Fe Kα complex, between 6.5 and 6.7 keV (see Fig. 6). Following previous results on Mrk 509 (Ponti et al. 2009, 2013; Yaqoob et al. 2003; Yaqoob & Padmanabhan 2004) and the features observed in NGC 4151 (XRISM Collaboration 2024), we added a broad Gaussian component that improves the fit ($\Delta C \sim 20$ for three parameters of interest). The line parameters are $E_b \simeq 6.49 \pm 0.15$ keV, a width of $\sigma_b \simeq 320 \pm 220$ eV, and $EW_b \simeq 90 \pm 50$ eV. The width of this feature ($v \sim 14\,800$ km/s) suggests an origin close to the SMBH, corresponding to $r \sim 50\, r_g$.

Interestingly, very similar results are obtained in the RR scenario (see the RR-I model in the lower panel of Table 3). Assuming a maximally spinning SMBH and a standard radial emissivity profile ($\epsilon \propto r^{-3}$), we derive a lower limit for the inner edge of the reflection disk of $r_{\rm in} \geq 27\, r_g$ (consistent with that obtained with the broad Gaussian), along with a low reflection fraction of $R \sim 0.17$ and a consistent broadening of the narrow FeK line.

4.1. Characteristics of the distant reflection

As shown in Table 3, the properties of the narrow emission line are consistent with an origin far from the SMBH in both the PC and the RR scenarios. To achieve a more robust physical characterization, we used the `MYTorus` model (Murphy & Yaqoob 2009; Yaqoob 2012) to account for this component in the PC scenario. `MYTorus` was in fact specifically designed for modeling the X-ray spectra of AGNs and their associated fluorescent lines originating in the dusty torus. Specifically, we added the `MYTorusL` (Fe Kα and Fe Kβ fluorescent emission lines, latest available version) and `MYTorusS` (reflected continuum) components to the primary power-law continuum. We linked their column densities to ensure self-consistency and fixed the inclination angle at $\Theta = 0°$, thereby assuming the matter lies out of the line of sight. Not only does `MYTorusL` reproduce the narrow Fe line profile (similar to `zFeklor`), but it also crucially ensures proper treatment of the Compton shoulder. The photon index of the `MYTorus` components was tied to that of the primary power law to maintain a uniform spectral slope. Since a preliminary Gaussian fit showed the narrow Fe line energy to be consistent with 6.4 keV, we fixed the redshift of the `MYTorus` components to that of Mrk 509, assuming no additional bulk motion. Finally, to test for line broadening, we applied a Gaussian smoothing kernel (`gsmooth` in XSPEC) to the `MYTorusL` component.

As shown in Fig. 7, the material responsible for the narrow emission lines (Fe Kα and Fe Kβ) must be located far from the SMBH, given that the line broadening is on the order of $\sigma = 10 \pm 5$ eV. This corresponds to a velocity of $v \sim 1000 \pm 500$ km s^{-1} (FWHM), a result that is well in agreement with that obtained using the zFeklor models and implying a distance on parsec scales for a SMBH with a mass of $M \sim 10^8\, M_\odot$ (Peterson et al. 2004; Li et al. 2024). This result strongly supports the hypothesis that the Fe K lines originate in the torus (Antonucci 1993).

On the other hand, the column density of this component is relatively lower ($N_H \sim 10^{23}$ cm^{-2}) than the average value ($N_H \sim 10^{24}$ cm^{-2}) found in samples of Compton-thin AGNs using *NuSTAR*. However, they are in good agreement with the lower end of the column densities measured for the Compton-thin sources in

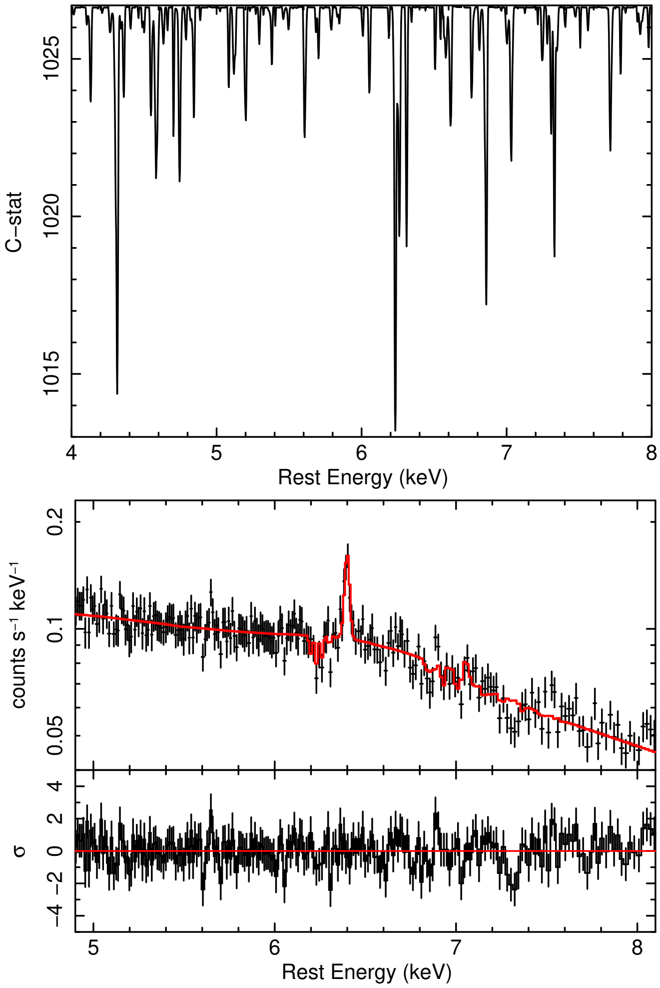

Fig. 9. *Upper panel*: Confidence contours (rest-frame energies) from the blind search for possible absorption features (see Sect. 4.2). *Lower panel*: Zoom-in on the spectral range where the strongest feature (absorption line at $E = 6.230^{+0.005}_{-0.020}$ keV) is measured.

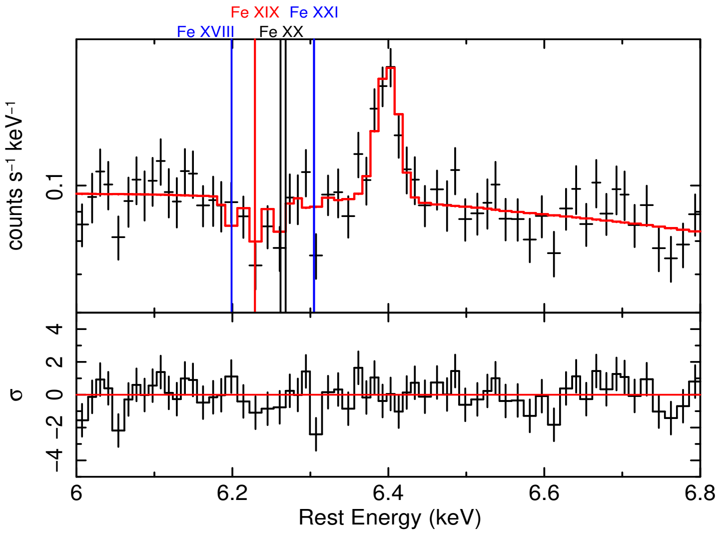

Fig. 10. 6.0–6.8 keV zoom-in on the spectral range where the strongest features from ionized gas are measured (model n8 in Table 3). The features measured in the 6.1–6.4 keV range are due to the Fe XVIII–Fe XXI lines.

the sample (Zhao et al. 2021). It is worth noting here that adding `MYTorus` in the RR scenario does not meaningfully improve the fit.

4.2. An infalling partial absorber

As described in the previous sections, a partial absorber of the primary emission is able to model the data well in both the PC and RR scenarios. As shown in Fig. 8 (PC scenario), some spectral features remain visible in the spectrum of Mrk 509, a trend also observed in the RR case. In particular, possible absorption features can be identified at $E \sim 4.2$, 6, 7 and, possibly, at 8–9 keV. When all these features are modeled with a Gaussian absorption line of fixed width ($\sigma = 5$ eV), the statistically strongest line is detected at $E = 6.230^{+0.005}_{-0.020}$ keV (see Fig. 9 for the PC case). This addition improves the fit by $\Delta C \sim 13$ in both scenarios.

To assess the importance of this absorption feature, we employed the small sample Akaike information criterion (AIC, Akaike 1974). Specifically, we computed the change in AIC (ΔAIC) when the line is removed from the model. A ΔAIC below -2 provides strong evidence that the feature is required, while a value below -10 would indicate it is essential for explaining the data. In our case, ΔAIC ~ -9 suggests the presence of this absorption line. Furthermore, a closer inspection of the ~6 keV region suggests a more complex structure, with possible multiple dips between the 6.0 and 6.1 keV rest frame (see the lower panel of Fig. 9).

Given the apparent complexity of the absorption feature, we used photoionized absorber models as a partial covering component to fit the absorption feature at ~6 keV. We created grid tables using the XSTAR code (Kallman & Bautista 2001) with an ionizing luminosity of $L_{1-1000\,\mathrm{Ry}} \approx 3.1\times10^{45}$ erg s^{-1} (see Sect. 4) and, following Petrucci et al. (2018), a SED dominated by a warm-plus hot-corona component tuned to the *XMM-Newton* and *NuSTAR* data (Missaglia et al. in prep.).

As a first step, we focused on the PC case and assumed a density of $n = 10^8$ cm^{-3} for the intervening gas, consistent with the absorber located at sub-parsec scales, comparable to the BLR. This is, for instance, supported by the unified stratification models of AGN winds (e.g., Tombesi et al. 2013; Gofford et al. 2013; Reeves et al. 2018; Serafinelli et al. 2019) and density diagnostics using metastable lines in similar Seyfert galaxies that typically yield $n \geq 10^8$ cm^{-3} for the high-ionization phases (e.g., Mao et al. 2017). Moreover, following the estimate obtained in Sect. 4 for the PC case, we also tested a density of $n \sim 10^{10}$ cm^{-3}, assuming that the matter emitting the broad Fe line is somehow linked to the material causing the partial absorption. In both scenarios, we fixed the matter turbulence to $v_{\mathrm{turb}} = 100$ km s^{-1} since the feature seems narrow (see Fig. 9). Models n8 and n10 and RR-n8 in Table 3 report the results obtained using these XSTAR grids. These models significantly improved the quality of the fit in both scenarios and provided a best-fit result with an absorbing gas density of $n = 10^8$ cm^{-3} and $\log\xi \sim 2.5$ (see models n8 and RR-n8 in Table 3 and Fig. 10).

As a consistency check, we also tested a different photoionized model, namely the PHASE model, based on CLOUDY (Ferland et al. 1998). This model is designed to reproduce absorption features from an ionized plasma, where the central source emits an ionizing continuum with gas clouds intercepting the line of sight (model Ph in the upper part of Table 3). Although it provides poorer statistical fit to the data compared to the XSTAR grid, the PHASE model yields consistent properties for the absorbing gas.

Table 3. Partial covering models.

Model	Γ	$N_{\rm H,torus}$ (10^{23} cm^{-2})	C_f	σ_n (eV)	$E_{\rm Fe,b}$ (keV)	σ_b (eV)	EW$_b$ (eV)	$N_{\rm H,pc}$ (10^{23} cm^{-2})	$\log\xi$	$z_{\rm obs}$	C/d.o.f.	ΔAIC
I	$1.84^{+0.08}_{-0.08}$	$1.00^{+0.12}_{-0.07}$	$0.32^{+0.19}_{-0.17}$	$10.2^{+4.5}_{-4.3}$	$6.489^{+0.116}_{-0.148}$	324^{+224}_{-179}	87^{+52}_{-49}	$1.44^{+0.47}_{-0.52}$			1917.2/1988	
n8	$1.80^{+0.07}_{-0.06}$	$0.98^{+0.12}_{-0.07}$	$0.29^{+0.15}_{-0.13}$	$10.1^{+4.6}_{-4.4}$	$6.502^{+0.193}_{-0.131}$	456^{+150}_{-127}	125^{+55}_{-51}	$3.82^{+1.50}_{-1.30}$	$2.52^{+0.12}_{-0.12}$	$0.0744^{+0.0005}_{-0.0005}$	1898.7/1986	15.2
n10	$1.81^{+0.10}_{-0.07}$	$0.99^{+0.03}_{-0.03}$	$0.30^{+0.16}_{-0.18}$	$10.2^{+4.6}_{-4.4}$	$6.506^{+0.184}_{-0.135}$	452^{+254}_{-130}	120^{+57}_{-53}	$3.89^{+1.63}_{-2.69}$	$2.45^{+0.27}_{-0.14}$	$0.0744^{+0.0005}_{-0.0005}$	1904.1/1986	9.1
Ph	$1.82^{+0.11}_{-0.10}$	$0.93^{+0.03}_{-0.03}$	$0.31^{+0.20}_{-0.17}$	$9.2^{+4.6}_{-4.3}$	$6.394^{+0.094}_{-0.087}$	313^{+113}_{-91}	88^{+53}_{-46}	$3.88^{+1.34}_{-1.23}$	$2.86^{+0.27}_{-0.14}$	$0.0735^{+0.0008}_{-0.0008}$	1906.5/1986	6.7
Model	**Γ**	**$N_{\rm H,pc}$ (10^{23} cm^{-2})**	**$\log\xi$**	**$z_{\rm obs}$**	**C_f**	**σ_b (eV)**	**EW (eV)**	**R**	**r$_{\rm in}$ (r$_g$)**	**$\log\xi$**	**C/d.o.f.**	**ΔAIC**
RR-I	$1.83^{+0.05}_{-0.04}$	$1.51^{+0.37}_{-0.37}$			$0.34^{+0.06}_{-0.03}$	$10.2^{+4.9}_{-4.6}$	29^{+24}_{-10}	$0.17^{+0.10}_{-0.03}$	≥ 27	$2.82^{+0.22}_{-0.13}$	1921.2/1988	
RR-n8	$1.72^{+0.02}_{-0.04}$	$3.67^{+1.52}_{-1.07}$	$2.53^{+0.08}_{-0.08}$	$0.0744^{+0.0005}_{-0.0005}$	$0.24^{+0.10}_{-0.12}$	$10.8^{+4.8}_{-4.3}$	28^{+12}_{-10}	$0.28^{+0.08}_{-0.06}$	53^{+73}_{-27}	$3.15^{+0.20}_{-0.22}$	1906.1/1986	11.1

Notes. *Upper table. PC models*: Col. I: Model name; Col. II: Photon index; Col. III: Column density of the distant reflector; Col. IV: Covering factor; Col. V: Width of the MYTorus line (gsmooth σ); Col. VI: Energy of the broad Gaussian line in emission; Col. VII: Width of the broad Gaussian line; Col. VIII: Equivalent width of the broad Gaussian line; Col. IX: Column density of the partial covering component; Col. X: Ionization factor; Col. XI: Observed redshift of the ionized absorber; Col. XII: Cash statistics over degrees of freedom; Col. XIII: AIC. *Lower table. RR models*: Col. I: Model name; Col. II: Photon index; Col. III: Column density of the partial covering component; Col. IV: Ionization factor of the partial covering component; Col. V: Observed redshift of the ionized absorber; Col. VI: Covering factor; Col. VII: Width of the narrow Gaussian line; Col. VIII: Equivalent width of the narrow Gaussian line; Col. IX: Reflection fraction parameter; Col. X: Inner radius of the accretion disk; Col. XI: Ionization factor of the relativistic reflection component; Col. XII: Cash statistics over degrees of freedom; Col. XIII: AIC. Model I: TBabs(zTBabs × constant(zpl + zgauss) + ((1 + constant) × (gsmooth × MTL + constant × MTS) + constant(zpl + zgauss)); n8: TBabs(XSTARn8 × constant(zpl + zgauss) + ((1 + constant) × (gsmooth × MYTL + MYTS)) + constant(zpl + zgauss)); n10: same as n8 with a different XSTAR table (see Section 4.2); Ph: TBabs(phase(zpl + zgauss) + (1 + constant) × (gsmooth × MYTL + MYTS) + constant(zpl + zgauss)); RR-I: TBabs × zTBabs(relxill + zfeklor) + constant × TBabs × relxill; RR-n8: TBabs × XSTARn8(relxill + zfeklor) + constant × TBabs × relxill.

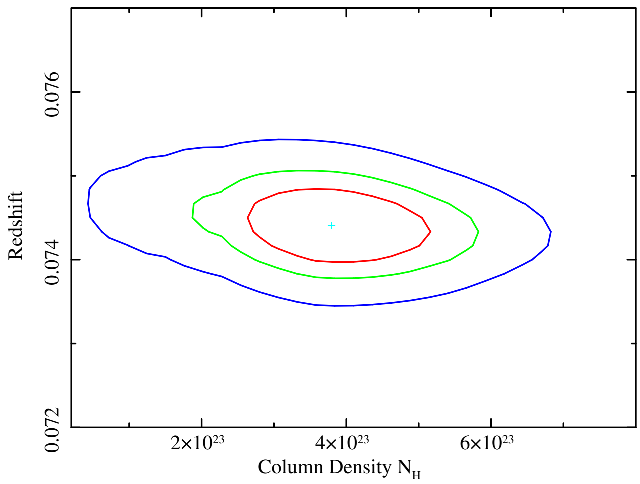

Fig. 11. *Upper panel*: 99%, 90%, and 68% confidence contours for the z vs. N_H parameters obtained using model n8 in Table 3.

Interestingly, by anchoring the models to the absorption features observed between ~6–7 keV (see Fig. 11), all the above models imply that the matter causing the ionized absorption is measured at a redshift of $z_{\rm obs} \sim 0.074$ (see the lower panel of Fig. 11). Since this finding is higher than the systemic redshift of Mrk 509 ($z_{\rm sou} = 0.034 \pm 0.001$), it could–if confirmed–indicate that the absorbing matter is infalling toward the central SMBH. In this energy range, the lines are primarily due to Fe XVIII–Fe XXI transitions.

To further test the significance of the infalling scenario, we performed Monte Carlo simulations under the PC scenario. Starting from the partial covering model (model I) presented in Table 3, we performed a suite of 1500 simulations of *XRISM*/Resolve spectra. These simulations were conducted using the rmf and arf generated for the data analysis, as previously described. To maintain consistency with the observational constraints, each simulated dataset was assigned an exposure time identical to that of the original observation. Subsequently, each of the 1500 simulated spectra was fitted using both the baseline Model I and the alternative model n8. For the model n8 fits, the ionization parameter was allowed to vary within the $\log(\xi/{\rm erg\,cm\,s^{-1}}) = 1.5$–$4.0$ range, while the observed redshift was free to fluctuate between $z = -0.2$ and $z = 0.2$. To ensure that each single fit did not stack in local minima, we forced the procedure to search for the errors on all free parameters multiple times before and after running the steppar command on the ionization parameter, the redshift, the column density of the ionized absorber, and the continuum-free parameters. For every simulated dataset, we recorded the value of the C-statistic for both models to calculate the difference, $\Delta(C)$, which provides the statistical basis for our cumulative distribution analysis presented in Fig. 12. According to this test, our results have a significance of ~3.6σ.

The current model produces residuals at a rest-frame energy of $E \sim 7.3$ keV (see Fig. 9). Adding a simple Gaussian absorption line yields a marginal improvement to the fit ($\Delta C \sim 14$ for three additional free parameters). Nevertheless, the centroid energy of this feature ($E \sim 7.31$ keV, $\sigma \sim 40$ eV, and $EW \sim 14$ eV) is perfectly consistent with previous findings (Ponti et al. 2009). If identified with highly ionized iron such as Fe XXVI this absorption feature would indicate an outflowing wind with a velocity on the order of 13 500 km/s.

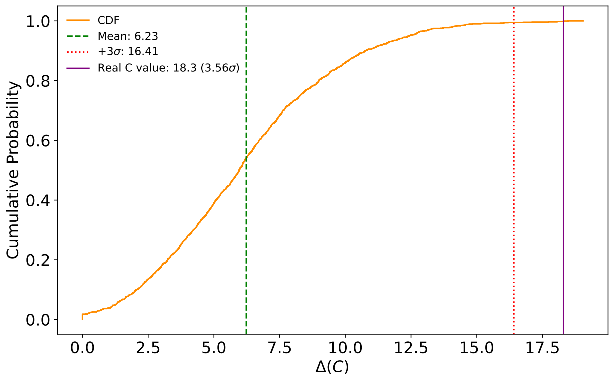

Fig. 12. Cumulative distribution of the ΔC statistic derived from 1500 Monte Carlo simulations, assuming Model I (see Table 2) as the null hypothesis. Synthetic *XRISM*/Resolve spectra were generated matching the exposure time of the real observation. For each simulation, ΔC is defined as the difference in the C-statistic between the best fits obtained modeling the simulated datasets with Model I and Model n8 in Table 2. The vertical green line indicates the mean simulated ΔC, while the red line marks the 3σ confidence threshold. The purple line represents the ΔC value observed in the real data.

It is interesting to note that the partial absorber characteristics yield completely consistent results when using the RR baseline model instead of the PC scenario. As reported in the lower part of Table 3, utilizing an ionized rather than cold absorber significantly improves the fit ($\Delta C = 15$ for two additional free parameters). More importantly, we obtain exactly the same properties for the absorber in terms of both its ionization state and velocity.

Finally, we tested the two scenarios by incorporating the *NuSTAR* data for observation 1 (performed within the Resolve pointing; see Fig. 1) and for observations 1 and 2 in the 10–60 keV range. From a statistical point of view, the two models perform identically, and the resulting parameters are fully consistent with those obtained using the Resolve data alone. The only notable difference lies in the cross-calibration constant between *XRISM*/Resolve and *NuSTAR*. In the PC case, we obtain a cross-calibration constant of $c_r = 1.08 \pm 0.05$, which is well in agreement with previous findings (Xrism Collaboration 2025b). Conversely, in the RR case, we measure a higher constant of $c_r = 1.21 \pm 0.10$

5. Discussion

The *XRISM*/Resolve spectrum of Mrk 509 displays the signatures of a complex structure at Fe K line energies. In particular, we detected:

- a narrow Fe Kα component, most likely arising from the putative torus;
- a relativistic or broad Fe Kα emission line originating from a region close to the central SMBH;
- spectral features consistent with a partial absorber, potentially associated with an infalling flow, although this interpretation remains model-dependent.

We estimate the dust sublimation radius for Mrk 509 to be $R_{\rm sub} \approx 0.74$ pc, using the scaling relation in Barvainis (1987) for graphite grains with a sublimation temperature of $T_{\rm sub} \approx 1500$ K and a bolometric luminosity of $L_{\rm bol} \approx 3.2 \times 10^{45}$ erg s^{-1} (Kaastra et al. 2012; Detmers et al. 2011). In comparison, the measured width of the narrow Fe Kα core ($\sigma_E \approx 10$ eV) corresponds to a virial emission radius of $R_{\rm FeK} \approx 2.0$ pc, assuming a black hole mass of $M_{\rm BH} \sim 1.02 \times 10^8\,M_\odot$ (Li et al. 2024). This places the bulk of the neutral iron emission outside the sublimation boundary ($R_{\rm FeK} \sim 2.7 R_{\rm sub}$), indicating that the fluorescent reflector is located within the body of the dusty torus rather than at its innermost wall. This geometry is consistent with clumpy torus scenarios where X-ray fluorescence arises from cold, dusty clouds that are sufficiently shielded from the central engine (Ramos Almeida & Ricci 2017).

As presented in Sect. 4, the best modeling of the data is obtained using a broad Fe emission detected at $E \approx 6.5 \pm 0.15$ keV, with a width of $\sigma \approx 450 \pm 150$ eV, which implies a velocity dispersion of $\sigma_v \approx 21\,000$ km s^{-1}. Adopting the virial assumption and the same black hole mass, we estimate an emission radius of $R_{\rm broad} \approx 0.001$ pc (~30–120 r_g). This places the production region roughly three orders of magnitude closer to the central engine than the dusty torus, consistent with the typical spatial scales of the BLR and the outer accretion disk. These spectral parameters are statistically consistent with those reported in Ponti et al. (2013) based on long *XMM-Newton* observations ($E = 6.43 \pm 0.01$ keV and $\sigma = 0.22 \pm 0.05$ keV). Notably, this physical scale is perfectly corroborated by the scenario in which the broad line originates from the relativistic reflection of the accretion disk; when explicitly modeled as disk reflection, we derive a lower limit of $r \geq 27\,r_g$ for the inner emission radius in excellent agreement with the virial estimate.

Our results for Mrk 509 align remarkably well with the emerging picture of the central engine revealed by recent *XRISM* observations of other Type 1 AGNs. In NGC 4151, the *XRISM* Collaboration (XRISM Collaboration 2024) identified an intermediate Fe Kα component originating from the outer accretion disk or the BLR transition region ($r \sim 50$–$500\,r_g$). This spatial scale is directly comparable to the $r \sim 30$–$120\,r_g$ region we derive for Mrk 509. XRISM Collaboration (2024) interpret this feature as potentially arising either from a warp in the accretion disk–which would locally enhance the illuminated solid angle–or from the base of a disk wind. It is worth noting that a similar wind scenario has recently been proposed for NGC 1068 (Grafton-Waters et al. 2021; Bianchi et al. 2026).

This consistency extends to other sources. For NGC 3783, Mehdipour et al. (2025) found that the broad Fe K emission is significantly narrower than expected for reflection from the innermost stable circular orbit ($r \leq 10\,r_g$), instead favoring an origin at larger radii ($r \geq 20$–$50\,r_g$). However, this result has since been challenged by the relativistic modeling by Li et al. (2026). More recently, Kammoun et al. (2025) demonstrated that NGC 7213 exhibits a clear radial stratification. The authors resolved the Fe K complex into a narrow core and a broad, asymmetric component that mirrors the optical Hα profile, placing its origin at $r \sim 100\,r_g$. They interpret this as emission from the outer accretion disk, bridging the gap between the compact corona and the optical BLR.

These studies suggest that the canonical “broad” iron line–typically associated with extreme relativistic reflection from the inner few gravitational radii (e.g., as in MCG-6-30-15; Brenneman et al. 2025)–is not always clearly detectable in nearby Seyfert galaxies. Instead, emission components originating from a transition zone at $r \sim 50$–$100\,r_g$ are possibly measured. This region, which may connect the turbulent accretion disk to the launch site of the BLR winds, can be a ubiquitous feature of Seyfert galaxies, which microcalorimeters are now able to resolve.

The X-ray spectral analysis of Mrk 509 reveals that, regardless of the specific ionization state of the absorbing matter, the modeling consistently requires a covering factor of $C_f \sim$

30% (see Table 3). To interpret the physical implications of this obscuration, we assumed a slab geometry for the primary X-ray continuum, consistent with recent X-ray polarimetric findings from *IXPE* (e.g., Gianolli et al. 2023; Pal et al. 2023; Marinucci et al. 2022) and with the theoretical framework of a disk-corona system proposed by Haardt & Maraschi (1993) and Haardt et al. (1994).

Assuming a typical coronal radius of $R_{\rm src} = 10\,r_{\rm g}$ (Risaliti et al. 2007; Chartas et al. 2009; Fabian et al. 2009; Wilkins & Fabian 2011) for a SMBH with the same mass of Mrk 509, we obtain $r_{\rm g} \approx 1.5 \times 10^{13}$ cm; thus, the physical source radius of the corona is $R_{\rm src} \approx 1.5 \times 10^{14}$ cm. To reproduce the observed covering factor of ~30% (interpreting C_f as the area ratio), the individual cloudlet or obscuring structure must have a characteristic transverse diameter of $D_{\rm c} \approx 1.6 \times 10^{14}$ cm (i.e., $\approx 10\,r_g$, a value consistent with that estimated for the "bullets" in PDS 456, Xrism Collaboration 2025a). Combining the measured column density of the absorber, $N_{\rm H} \sim 1\text{–}4 \times 10^{23}\,{\rm cm}^{-2}$, with these physical dimensions, and assuming a simple spherical or shell-like geometry where the path length is comparable to the diameter ($L \approx D_{\rm c}$), we estimate a volume density of $n \approx N_{\rm H}/D_{\rm c} \approx 1\text{–}7 \times 10^9\,{\rm cm}^{-3}$ (taking into account the 90% errors in the absorber column density and the covering factor).

This estimate, however, assumes a uniform sphere and a central line of sight. When accounting for off-center sightlines (intercepting a chord rather than the full diameter) and the expected density stratification within the gas, this average value becomes a strict lower limit. The actual local density within the core of the absorber is expected to be significantly higher, likely on the order of $n \sim 10^{10}\,{\rm cm}^{-3}$.

We can attempt to independently constrain these physical parameters by considering the ionization state of the absorber, bearing in mind the uncertainties in the detection. The data favor the presence of an ionized phase ($\log(\xi/{\rm erg\,cm\,s^{-1}}) \sim 2.5$; see Table 3) which, in the best-fit model, appears to possess a significant inflow velocity of $v_{\rm in} \approx 11\,000\,{\rm km\,s^{-1}}$. If we assume that the gas dynamics are solely governed by the gravitational potential of the central SMBH, this free-fall velocity would place the material at a distance of $r \approx 1500\,r_{\rm g}$ ($\approx 2.2 \times 10^{16}$ cm). Using this distance and the observed ionization parameter, we estimate a local gas density of $n \approx 2 \times 10^{10}\,{\rm cm}^{-3}$. When accounting for the outward radiation pressure, the effective gravitational acceleration is reduced by a factor of $(1 - \Gamma_{\rm rad})$ (e.g., Proga & Kallman 2004; King & Pounds 2015), where $\Gamma_{\rm rad} \sim 0.25$ is the Eddington ratio for Mrk 509, yielding $r \approx 1150\,r_{\rm g}$ and $n \approx 3.5 \times 10^{10}\,{\rm cm}^{-3}$.

This value is remarkably consistent with the lower limit derived from the geometrical constraints described above. This tentatively suggests a scenario where the absorber might consist of dense, BLR-like material located within the inner few thousand gravitational radii. In this picture, the gas participates in a non-Keplerian inflow, fragmented into blobs rather than forming a smooth, continuous flow, consistent with failed wind clumps "raining" back toward the central engine (e.g., Ghisellini et al. 2004; Proga & Kallman 2004; Giustini & Proga 2019). It is worth noting that detailed optical studies of Mrk 509's BLR properties indicate clouds with radial motion components, though in outflow (GRAVITY Collaboration 2024).

It is worth noting a tension between the spectral modeling results and the physical estimates derived above. Specifically, the fit statistically prefers model n8 ($n = 10^8\,{\rm cm}^{-3}$) over model n10 (see Table 3), even though the latter employs a density ($n = 10^{10}\,{\rm cm}^{-3}$) that is consistent with the geometrical constraints and the virial requirements for the inflow. First of all, it is important to stress that the statistical difference between these two solutions is not large ($\Delta C = 5.2$), which suggests that the data do not rule out the high-density scenario on statistical grounds alone. On the other hand, this apparent discrepancy can be reconciled assuming that the absorber possesses a "cometary" structure (Maiolino et al. 2010; Risaliti et al. 2011). In this scenario, the absorber relies on a dense, compact core. As this core plunges inward, the intense radiation field ablates its outer layers, generating a diffuse, elongated tail with low-density material. The radiation pressure directs this tail outward, effectively pointing it toward the observer. Consequently, our line of sight passes through the full length of this lower-density tail before interacting with the core. The spectral modeling is therefore weighted toward the physical conditions of the extended tail, while the measured column density ($N_H \sim 10^{23}\,{\rm cm}^{-2}$) results from integrating along this extended path length ($L \sim 10^{15}$ cm), consistent with the proposed geometry.

The energetic implications of these potential "raining" clumps are nonnegligible. Traveling at a free-fall velocity of $v_{\rm in} \approx 11\,000\,{\rm km\,s^{-1}}$, a single clump carries significant kinetic energy. Adopting the derived physical diameter of $D_{\rm c} \approx 1.6 \times 10^{14}$ cm (implying a spherical volume of $V \approx 2.1 \times 10^{42}\,{\rm cm}^3$) and a fiducial density of $n = 10^{10}\,{\rm cm}^{-3}$, we estimate a single clump mass of $M_{\rm c} \approx 3.6 \times 10^{28}$ g (assuming $M_c \approx nVm_p$). Consequently, the kinetic energy associated with this structure is $K = \frac{1}{2} M_{\rm c} v_{\rm in}^2 \approx 2 \times 10^{46}$ erg.

Although the kinetic energy carried by a single cloudlet may be substantial, it represents a transient energy injection. Given the average bolometric luminosity of the source ($L_{\rm bol} \sim 3 \times 10^{45}\,{\rm erg\,s^{-1}}$), the energy released by the accretion of a single clump would sustain the AGN output for only a few seconds (assuming efficient thermalization). Therefore, in order for this "raining" mechanism to have a significant, sustained impact on the global energy budget of the system, such accretion events cannot be sporadic. On the other hand, these cloudlets impacting the disk may play a crucial dynamical role beyond merely replenishing the fuel supply. The collision of such massive, dense clumps with the accretion disk may induce local instabilities and density perturbations within the flow. These stochastic inhomogeneities can then propagate inward through the disk on viscous timescales, effectively acting as the physical "seeds" for the propagating fluctuations model (e.g., Lyubarskii 1997; Arévalo & Uttley 2006). In this scenario, the raining material may contribute to the intrinsic variability of the accretion flow, providing a mechanism to explain the observed broadband timing properties, including the characteristic time lags detected between different X-ray energy bands (De Marco et al. 2013). It is finally worth mentioning here that the possible detection of a concurrent UFO signature in the form of an absorption line at $E \sim 7.3$ keV (see also Ponti et al. 2009) is in agreement with the scenario depicted in Elvis (2017) for the formation of BLR in AGNs.

6. Conclusions

In this work, we presented a detailed spectral analysis of the Seyfert 1 galaxy Mrk 509, focusing on the high-resolution X-ray spectrum obtained by the *XRISM*/Resolve calorimeter, complemented by simultaneous *NuSTAR* and *XMM-Newton* observations. Our analysis leads to the following main conclusions:

– The Fe K complex decomposition: Thanks to *XRISM*'s unprecedented resolution, we successfully disentangled the various components of the Fe K complex. We identified a narrow neutral Fe Kα core ($\sigma < 10$ eV), originating from distant material consistent with the dusty torus (as modeled by MYTorus). Additionally, we required a broad emission component and modeled it using either a broad Gaussian in emission or a relativistic reflection, revealing that it must originate at $r \sim 30-120\,r_g$ from the central engine, consistent with the BLR or the outer accretion disk rather than the innermost regions.

– Partial covering versus pure relativistic reflection: We tested two scenarios to explain the spectral curvature and the 2–10 keV complexity. While a pure relativistic line can statistically reproduce the curvature, it yields a primary photon index ($\Gamma \sim 1.5-1.6$, see Table 2) that is quite flat than the average values for Seyfert galaxies. Conversely, a partial covering model (for both models n8 and RR-n8 in Table 3) retrieves a canonical photon index ($\Gamma \sim 1.7-1.8$).
– Potential indications of a "raining" absorber: The modeling suggests the presence of an ionized partial absorber ($\log(\xi/\mathrm{erg\,cm\,s^{-1}}) \sim 2.5$) which, under specific density assumptions ($n \approx 10^{8-10}\,\mathrm{cm^{-3}}$), is consistent with inflows at a high velocity of $v_{\rm in} \approx 11\,000\,\mathrm{km\,s^{-1}}$. If confirmed, the physical modeling places this absorber at $r \approx 1100-1500\,r_g$, consistent with a clumpy, fragmented flow. This is likely interpreted as "failed wind" clumps losing angular momentum and raining back toward the central black hole, possibly with a cometary-like shape.

Future monitoring with *XRISM* and *NewAthena* will be crucial to firmly confirm the existence and track the variability of these absorption features in Mrk 509 and in other sources. This is mandatory to firmly establish, if any, the possible connections between the infalling gas dynamics and the accretion flow that fuel the central SMBH in AGNs.

Acknowledgements. The authors are grateful to the anonymous referee for their careful reading of the manuscript and valuable feedback, which significantly strengthened this work. M.D., V.M., V.B., M.C., A.L., S.B., A.C., E.N., F.N., C.P., E.B. and A.T. acknowledge financial support from the Bando Ricerca Fondamentale INAF 2023, Large Program 1.05.23.01.06 ("The XRISM-to-XIFU (X2X) Agreement and Beyond: entering a new Era of High Resolution X-Ray Spectroscopy"). M.D, M.C. F.N and A.L. acknowledge financial support from PRIN MUR 2022 DRAGON 2022K9N5B4. E.B. acknowledges the support of the INAF GO grant "A JWST/MIRI MIRACLE: Mid-IR Activity of Circumnuclear Line Emission" and of the "Ricerca Fondamentale 2024" INAF program (mini-grant 1.05.24.07.01). P.O.P. acknowledges support from the CNES french spatial agency and from the ≪ Action Thématique Phénomèes Extrêmes et Multimessager ≫ of the Astronomy-Astrophysics National Programme from INSU/CNRS. C.P. is funded by INAF Large Grant 2023 BLOSSOM F.O. 1.05.23.01.13. R.S. acknowledges funding from the CAS-ANID grant number CAS220016.

References

Akaike, H. 1974, IEEE Trans. Automat. Control, 19, 716
Antonucci, R. 1993, ARA&A, 31, 473
Arévalo, P., & Uttley, P. 2006, MNRAS, 367, 801
Arnaud, K., Dorman, B., & Gordon, C. 1999, Astrophysics Source Code Library [record ascl:9910.005]
Barvainis, R. 1987, ApJ, 320, 537
Bianchi, S., Guainazzi, M., Matt, G., et al. 2009, A&A, 495, 421
Bianchi, S., Vander Meulen, B., Bertola, E., et al. 2026, A&A, 710, A294
Braito, V., Reeves, J. N., Matzeu, G. A., et al. 2018, MNRAS, 479, 3592
Brenneman, L. W., Wilkins, D. R., Ogorzałek, A., et al. 2025, ApJ, 995, 200
Cappi, M. 2006, Astron. Nachr., 327, 1012
Cappi, M., Tombesi, F., Bianchi, S., et al. 2009, A&A, 504, 401
Chartas, G., Brandt, W. N., Gallagher, S. C., et al. 2002, ApJ, 579, 169
Chartas, G., Kochanek, C. S., Dai, X., et al. 2009, ApJ, 693, 174
Chartas, G., Cappi, M., Vignali, C., et al. 2021, ApJ, 920, 24
Collin, S., Kawaguchi, T., Peterson, B. M., & Vestergaard, M. 2006, A&A, 456, 75
Dadina, M. 2007, A&A, 461, 1209
Dadina, M. 2008, A&A, 485, 417
Dadina, M., Cappi, M., Malaguti, G., et al. 2005, A&A, 442, 461
Dadina, M., Vignali, C., Cappi, M., et al. 2018, A&A, 610, L13
Dauser, T., Garcia, J., Parker, M. L., et al. 2014, MNRAS, 444, L100
De Marco, B., Ponti, G., Cappi, M., et al. 2013, MNRAS, 431, 2441
Detmers, R. G., Kaastra, J. S., Steenbrugge, K. C., et al. 2011, A&A, 534, A38
Elvis, M. 2017, ApJ, 847, 56
Fabian, A. C., Iwasawa, K., Reynolds, C. S., & Young, A. J. 2000, PASP, 112, 1145
Fabian, A. C., Zoghbi, A., Ross, R. R., et al. 2009, Nature, 459, 540
Ferland, G. J., Korista, K. T., Verner, D. A., et al. 1998, PASP, 110, 761
García, J. A., Fabian, A. C., Kallman, T. R., et al. 2016, MNRAS, 462, 751
Gaspari, M., Tombesi, F., & Cappi, M. 2020, Nat. Astron., 4, 10
Ghisellini, G., Haardt, F., & Matt, G. 2004, A&A, 413, 535
Gianolli, V. E., Kim, D. E., Bianchi, S., et al. 2023, MNRAS, 523, 4468
Gianolli, V. E., Bianchi, S., Petrucci, P.-O., et al. 2024, A&A, 687, A235
Giustini, M., & Proga, D. 2019, A&A, 630, A94
Giustini, M., Costantini, E., De Marco, B., et al. 2017, A&A, 597, A66
Gofford, J., Reeves, J. N., Tombesi, F., et al. 2013, MNRAS, 430, 60
Grafton-Waters, S., Branduardi-Raymont, G., Mehdipour, M., et al. 2021, A&A, 649, A120
GRAVITY Collaboration (Amorim, A., et al.) 2024, A&A, 684, A167
Haardt, F., & Maraschi, L. 1993, ApJ, 413, 507
Haardt, F., Maraschi, L., & Ghisellini, G. 1994, ApJ, 432, L95
Harrison, F. A., Craig, W. W., Christensen, F. E., et al. 2013, ApJ, 770, 103
Heckman, T. M., & Best, P. N. 2014, ARA&A, 52, 589
Hölzer, G., Fritsch, M., Deutsch, M., Härtwig, J., & Förster, E. 1997, Phys. Rev. A, 56, 4554
Huchra, J., Latham, D. W., da Costa, L. N., et al. 1993, AJ, 105, 1637
Ishisaki, Y., Kelley, R. L., Awaki, H., et al. 2025, J. Astron. Telesc. Instrum. Syst., 11, 042023
Jansen, F., Lumb, D., Altieri, B., et al. 2001, A&A, 365, L1
Kaastra, J. S., Detmers, R. G., Mehdipour, M., et al. 2012, A&A, 539, A117
Kallman, T., & Bautista, M. 2001, ApJS, 133, 221
Kammoun, E., Kawamuro, T., Murakami, K., et al. 2025, ApJ, accepted [arXiv:2510.24971]
King, A., & Pounds, K. 2015, ARA&A, 53, 115
Kormendy, J., & Ho, L. C. 2013, ARA&A, 51, 511
Kumari, N., Pal, M., Naik, S., et al. 2021, PASA, 38, e042
Laha, S., Reynolds, C. S., Reeves, J., et al. 2021, Nat. Astron., 5, 13
Li, Y.-R., Hu, C., Yao, Z.-H., et al. 2024, ApJ, 974, 86
Li, C., Kaastra, J. S., Gu, L., et al. 2026, A&A, 706, A255
Longinotti, A. L., Sim, S. A., Nandra, K., et al. 2007, MNRAS, 374, 237
Lyubarskii, Y. E. 1997, MNRAS, 292, 679
Maiolino, R., Risaliti, G., Salvati, M., et al. 2010, A&A, 517, A47
Mao, J., Kaastra, J. S., Mehdipour, M., et al. 2017, A&A, 607, A100
Marinucci, A., Muleri, F., Dovciak, M., et al. 2022, MNRAS, 516, 5907
Matzeu, G. A., Reeves, J. N., Nardini, E., et al. 2016, MNRAS, 458, 1311
Matzeu, G. A., Reeves, J. N., Braito, V., et al. 2017, MNRAS, 472, L15
Matzeu, G. A., Brusa, M., Lanzuisi, G., et al. 2023, A&A, 672, A24
Mehdipour, M., Branduardi-Raymont, G., Kaastra, J. S., et al. 2011, A&A, 534, A39
Mehdipour, M., Kaastra, J. S., Eckart, M. E., et al. 2025, A&A, 699, A228
Middei, R., Bianchi, S., Petrucci, P. O., et al. 2019, MNRAS, 483, 4695
Mizumoto, M., Reeves, J. N., Braito, V., et al. 2026, ApJ, 997, 219
Murphy, K. D., & Yaqoob, T. 2009, MNRAS, 397, 1549
Nandra, K., & Pounds, K. A. 1994, MNRAS, 268, 405
Nandra, K., George, I. M., Mushotzky, R. F., et al. 1999, ApJ, 523, L17
Nandra, K., O'Neill, P. M., George, I. M., & Reeves, J. N. 2007, MNRAS, 382, 194
Nardini, E., Reeves, J. N., Gofford, J., et al. 2015, Science, 347, 860
Negrete, C. A., Dultzin, D., Marziani, P., et al. 2012, ApJ, 757, 62
Pal, I., Stalin, C. S., Chatterjee, R., et al. 2023, JApA, 44, 87
Peca, A., Koss, M. J., Serafinelli, R., et al. 2025, ApJ, 989, 84
Peterson, B. M., Ferrarese, L., Gilbert, K. M., et al. 2004, ApJ, 613, 682
Petrucci, P.-O., Paltani, S., Malzac, J., et al. 2013, A&A, 549, A73
Petrucci, P.-O., Ursini, F., De Rosa, A., et al. 2018, A&A, 611, A59
Piconcelli, E., Jimenez-Bailón, E., Guainazzi, M., et al. 2005, A&A, 432, 15
Ponti, G., Cappi, M., Vignali, C., et al. 2009, MNRAS, 394, 1487
Ponti, G., Cappi, M., Costantini, E., et al. 2013, A&A, 549, A72
Pounds, K., Reeves, J., O'Brien, P., et al. 2001, ApJ, 559, 181
Pounds, K. A., Reeves, J. N., King, A. R., et al. 2003, MNRAS, 345, 705
Proga, D., & Kallman, T. R. 2004, ApJ, 616, 688
Ramos Almeida, C., & Ricci, C. 2017, Nat. Astron., 1, 679
Reeves, J. N., Wynn, G., O'Brien, P. T., et al. 2002, MNRAS, 335, 126
Reeves, J. N., O'Brien, P. T., Braito, V., et al. 2009, ApJ, 701, 493
Reeves, J. N., Braito, V., Gofford, J., et al. 2014, ApJ, 780, 45
Reeves, J. N., Braito, V., Nardini, E., et al. 2018, ApJ, 854, L8

Ricci, C., Trakhtenbrot, B., Koss, M. J., et al. 2017, ApJS, 233, 17
Risaliti, G., Elvis, M., Fabbiano, G., et al. 2007, ApJ, 659, L111
Risaliti, G., Nardini, E., Salvati, M., et al. 2011, MNRAS, 410, 1027
Ross, R. R., & Fabian, A. C. 1993, MNRAS, 261, 74
Serafinelli, R., Tombesi, F., Vagnetti, F., et al. 2019, A&A, 627, A121
Shakura, N. I., & Sunyaev, R. A. 1973, A&A, 24, 337
Śniegowska, M., Marziani, P., Czerny, B., et al. 2021, ApJ, 910, 115
Tanaka, Y., Nandra, K., Fabian, A. C., et al. 1995, Nature, 375, 659
Tashiro, M., Watanabe, S., Maejima, H., et al. 2024, Proc. SPIE, 13093, 130931G
Tashiro, M., Kelley, R., Watanabe, S., et al. 2025, PASJ, 77, S1
Tombesi, F., Cappi, M., Reeves, J. N., et al. 2010, A&A, 521, A57
Tombesi, F., Cappi, M., Reeves, J. N., et al. 2011, ApJ, 742, 44
Tombesi, F., Cappi, M., Reeves, J. N., et al. 2013, MNRAS, 430, 1102
Wilkins, D. R., & Fabian, A. C. 2011, MNRAS, 414, 1269
XRISM Collaboration (Audard, M., et al.) 2024, ApJ, 973, L25
Xrism Collaboration (Audard, M., et al.) 2025a, Nature, 641, 1132
Xrism Collaboration (Audard, M., et al.) 2025b, A&A, 702, A147
Yaqoob, T. 2012, MNRAS, 423, 3360
Yaqoob, T., & Murphy, K. D. 2011, MNRAS, 412, 277
Yaqoob, T., & Padmanabhan, U. 2004, ApJ, 604, 63
Yaqoob, T., & Serlemitsos, P. 2005, ApJ, 623, 112
Yaqoob, T., McKernan, B., Kraemer, S. B., et al. 2003, ApJ, 582, 105
Zhao, X., Civano, F., Fornasini, F. M., et al. 2021, MNRAS, 508, 5176